ACS APPLIED NANO MATERIALS

www.acsanm.org

Article

Enhancement and Tunability of Plasmonic-Magnetic Hyperthermia through Shape and Size Control of Au:Fe_3O_4 Janus Nanoparticles

Esraa Samy Abu Serea, Iñaki Orue, José Ángel García, Senentxu Lanceros-Méndez, and Javier Reguera*

Cite This: *ACS Appl. Nano Mater.* 2023, 6, 18466−18479

Read Online

ACCESS | Metrics & More | Article Recommendations | Supporting Information

ABSTRACT: Nanohyperthermia therapies have appeared as a promising alternative for the treatment of diverse cancer tumors. Multifunctional nanosystems offer a step forward in these therapies. They harness more efficient and multistimuli hyperthermia for low-dose application, as well as supplementary functions for imaging, targeting, controlled release, and sensing. Among them, Janus Au:Fe_3O_4 nanoparticles (JNPs) are highly versatile and a prominent example for dual photo- and magnetothermia capabilities. To achieve the highest efficiencies of these nanomaterials, which allow low-dose applications, optimization in terms of size and shape is imperative. Here, we have expanded the synthesis of Janus nanostructures and carried out a systematic study to understand the structure−performance relationship and improve their hyperthermia efficiency. JNPs were synthesized by seed-mediated growth processes to obtain Janus nanostars (JNSs) and Janus nanospheres (JNSphs) with controlled sizes, together with initial heterodimers and indented F_3O_4 NPs. The hyperthermia abilities were then evaluated using AC magnetometry and under near-infrared laser irradiation. The results showed a clear effect of size and shape on the tuning of both magnetothermia and photothermia. Iron oxide size showed the biggest effect on magnetothermia, which could be tuned by the size and shape of the gold component. Likewise, for photothermia, JNSs offered the best performance and a clear correlation between the proximity of the plasmonic band to the irradiation source and their photothermal performance, modulated by the presence of iron oxide. A SAR_{max} of 3 kW g^{-1} for the strongest field and frequency tested, 0.48 kW g^{-1} for biological safety limits in magnetothermia, and 8.3 kW g^{-1} per W cm^{-2} of applied light for photothermia were obtained. The acquired results support the proper selection of the best JNPs for dual hyperthermia and allow one to set up the design rules for obtaining more efficient multifunctional nanosystems, opening new avenues toward advanced heating-based therapies.

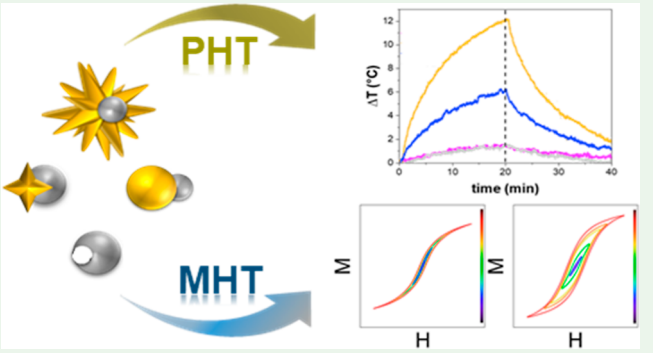

KEYWORDS: *plasmonic, magnetic hyperthermia, shape, size, control, Janus nanoparticles*

INTRODUCTION

Noninvasive thermal therapies are considered to be more efficient and have fewer harmful effects than conventional therapies. This is especially relevant for deeply embedded malignant tumors in organs that cannot be removed by surgery.[1−3] In other types of tumors, thermal therapies can also be utilized as coadjuvants to increase the susceptibility of cancer cells to radio- and chemotherapy via different heat sources such as lasers, ultrasounds, or microwaves. However, these methods can also harm healthy tissues situated in the proximity and between the target and the heat source.[4−7] Nanoparticle-based thermal therapies provide a solution to the limitations of traditional techniques.[8−13] One of the key advantages is that they can be directed to specific locations within the body using magnetic fields, targeting ligands, or passively through the enhanced-permeation-retention (EPR) effect.[14−16] The combination of such NP accumulation at the tumors and localized external stimuli limits the damage to the surrounding healthy tissue and the possible side effects.[17−22]

Among the hyperthermia treatments, there are two main modalities: photothermia and magnetothermia. Plasmonic (PNPs) and magnetic (MNPs) nanoparticles such as Au and iron oxide are considered excellent candidates for these heating-based applications, respectively.[23−26] Plasmonic Au NPs have outstanding optical properties, provided by their localized surface plasmon resonance (LSPR), with high light absorption and photothermal transduction. This feature, together with its chemical stability and biocompatibility,

Received: August 16, 2023
Accepted: September 21, 2023
Published: October 4, 2023

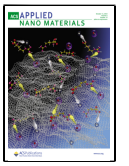

Scheme 1. Schematic Illustration of the Synthesis of Au/Fe_3O_4 JNPs with Structural Control through (A) Changing the Size of the Fe_3O_4 Component of JNPs via Variations in the Thermal Decomposition Method Followed by (B) Growing the Au Component for Different Sizes and Shapes by a Seed-Mediated-Growth Synthesis

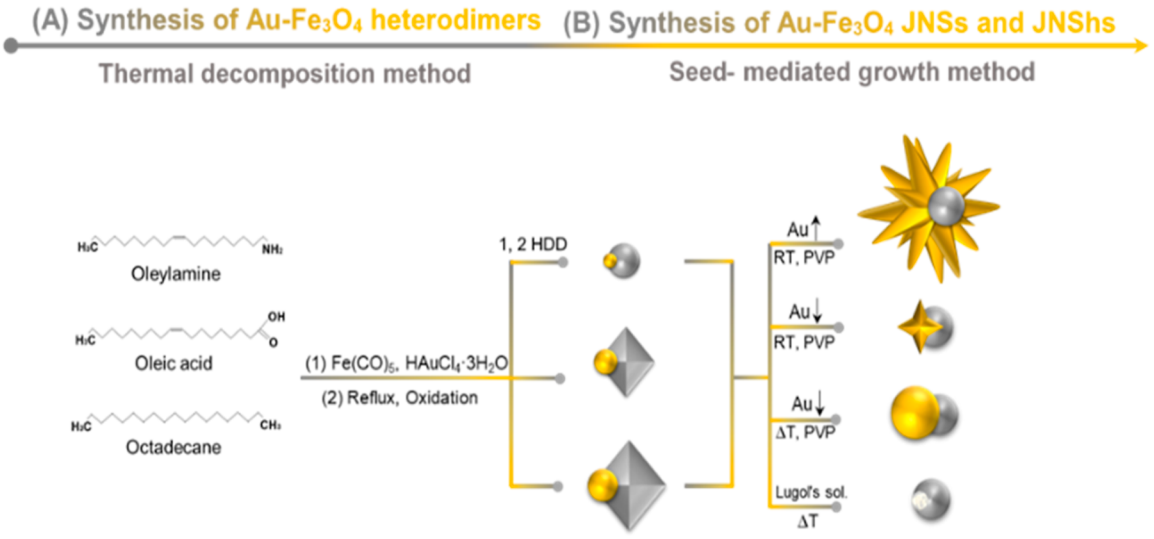

makes Au NPs excellent candidates for noninvasive thermal therapy.[27,28] Among the different types of Au NPs, Au nanostars have shown excellent light absorption and photothermal capabilities[3,29] that can be tuned by adjusting the width and length of the nanostar spikes.[30,31] Moreover, they can be grown using seed-mediated growth large-scale wet chemical methods from different types of Au seeds.[32] On the other hand, iron oxide NPs, have been demonstrated to be good energy-to-heat converters in the presence of an alternating magnetic field, offering high biocompatibility and biodegradation, in the long term, into endogenous iron.[33−35]

Despite their extraordinary capabilities, both hyperthermia techniques are characterized by well-known limitations. This includes the high dose needed for magnetothermia or the low penetration depth of photothermia, that even in the biological transparency window is limited to a centimeters scale. The development of nanohybrid platforms based on the combination of gold and iron oxide unites the advantages of each methodology. It offers a more complete and versatile platform that can create dual magnetic and plasmonic hyperthermia while acting as a contrast agent in multimodal imaging or enabling magnetic targeting.[36] In the case of hyperthermia, the dual system can offer adaptability to tumor type in terms of tissue and location and enhance the hyperthermia treatment due to additive and synergistic biological effects. All of it translates into a reduction of the nanoparticle (NPs) and physical stimulus dose to improve performance and decrease systemic toxicity.[23] A few works have shown NPs that combine the use of these two materials, including core−shell NPs, assemblies of NPs, or just nanoparticle aggregates.[36] We recently developed the synthesis of Janus nanostars (JNSs) with applicability as a dual nanoplatform for cancer treatment and imaging.[23,37−40] Although they have been shown to be promising candidates for tumor hyperthermia treatment, very little is known about how their parameters, in terms of size, shape, and component ratios, affect their efficiency to be used in hyperthermia treatment.

In the current work, we present the fabrication of Janus multifunctional magnetic-plasmonic NPs composed of two different domains of Au and Fe_3O_4 bound epitaxially (Scheme 1). The synthesis of the initial NPs (hereafter called heterodimers) was performed by variations of the thermal decomposition method,[41,42] which expanded the size of the Fe_3O_4 component from 10 to 30 nm. The formed Au−Fe_3O_4 heterodimers were then used as seeds to form different versions of NPs by the growth of the Au domain into several morphologies. They were formed as nanostars to form JNSs or as spheres of bigger size to form Janus nanospheres (JNSphs) and with tunable sizes by adjusting the seed to reagent-Au ratio, in this case from 18 to 75 nm. As a control, the Au of the heterodimer was etched to obtain indented Fe_3O_4 NPs with the same size and size distribution of the heterodimer Fe_3O_4 lobes. Tuning their shape as well as dimensions provides a wide range of characteristics in terms of magnetic and optical properties that can be adjusted to improve efficiency. In water dispersion, the heat conversion capabilities, such as specific absorption rate (SAR), were evaluated when exposed to either NIR laser at 785 nm (first biological window) or to an alternating magnetic field at three frequencies, 143, 350, and 732 kHz, and magnetic fields up to 80 mT. We showed that the relative sizes and morphology highly influence the structure−performance relationship and demonstrate the possibility of optimizing the morphologic and structural features for generating superior magnetic and photothermal efficiency. Thus, it paved the way for the implementation of low-dose heating-based therapies based on multifunctional nanoparticles.

EXPERIMENTAL SECTION

Chemicals. Iron pentacarbonyl $Fe(CO)_5$, 1-octadecene (ODE, 90%), oleylamine (70%), oleic acid (90%), 1,2-hexadecanediol (HDD, 90%), *N*,*N*-dimethylformamide (99.9%), polyvinylpyrrolidone (PVP) (M_W = 10 kg mol^{-1}), poly(isobutylene-*alt*-maleic anhydride) (M_w = 6000 g/mol), 1-dodecylamine, methoxypolyethylene glycol-acetic acid (PEG-COOH, M_W = 5 kg mol^{-1}), chloroform, 2-propanol, ethanol (absolute, ACS grade), and Lugol's solution were bought from Sigma-Aldrich. Hydrogen tetrachloroaurate trihydrate ($HAuCl_4 \cdot 3H_2O$, 99.99%) was purchased from Thermo-Fisher. All reagents were used as received without any further purification.

Synthesis of Gold−Iron Oxide Heterodimers with $d_{Fe_3O_4}$ = 10 nm. For a typical synthesis, in a three-neck flask, a solution containing

https://doi.org/10.1021/acsanm.3c03818
ACS Appl. Nano Mater. 2023, 6, 18466−18479

2.58 g of 1,2-hexadecanodiol, 2 mL of oleylamine, and 2 mL of oleic acid in 47 mL of 1-octadecane was stirred at 120 °C for 20 min under N_2 flow. Then, 0.3 mL of $Fe(CO)_5$ was injected at 120 °C, which produced a decrease in the solution temperature. After reaching 120 °C again, a freshly prepared gold mixture (40 mg of $HAuCl_4{\cdot}3H_2O$ dissolved in 0.5 mL of oleylamine and 3 mL of 1-octadecane) was injected and heated up to 310 °C at 3 °C/min. The system was aged under reflux for 90 min at 310 °C. The reaction mixture was cooled to room temperature followed by Fe-oxidation by exposing it to air. The final solution was cleaned three times by centrifugation (7000 rpm, 30 min) using 2-propanol to destabilize the sample and small quantities of chloroform (~1 mL) to disperse the NPs. The stock solution was dispersed in 5 mL of $CHCl_3$ and stored in the fridge.

Synthesis of Gold−Iron Oxide Heterodimers with $d_{Fe_3O_4}$ = 24 nm. A methodology similar to the case above was followed. In this case, 1,2-hexadecanodiol was not included in the reaction, and the quantity used was 20 mL of 1-octadecane; 20 mg of $HAuCl_4{\cdot}3H_2O$ and 0.08 mL $Fe(CO)_5$ were added at 120 and 150 °C, respectively. The reaction mixture was aged at 200 °C for 90 min and then at 300 °C for 1 h.

Synthesis of Gold−Iron Oxide Heterodimers with $d_{Fe_3O_4}$ = 30 nm. A methodology similar to the case of 24 nm heterodimers was followed with a change in the temperature profile. In this case, a further increase of the holding time to 2 h at 200 °C and then 90 min at 300 °C was applied. In a sequence of experiments, the iron oxide size was controlled by ending the reaction at different holding times and changing the relative amounts of surfactants. A summary of all synthesis conditions can be found in the Supporting Information, Table S1.

Synthesis of Star-Shaped Au−Fe_3O_4: JNSs. The synthesized NPs were initially modified by place-ligand exchange with PEG to improve their dispersibility in DMF. 21 mg of PEG-COOH was dissolved in 1 mL of chloroform, added dropwise to 50 μL of gold−iron oxide seeds, and then shaken for 30 min.

A solution containing $HAuCl_4{\cdot}3H_2O$ (1.092 mL, 50 mM) was added after the complete dissolution of 10 g of PVP in 200 mL of DMF. After 6 min of stirring of the reaction mixture (prereduction of the Au precursor), the solution containing the seeds was added. After injecting the required volume of seeds solution, the reaction mixture was left stirring for 2 h until the solution turned blue.

Different NPs were obtained by growing the Au domain in different sizes of JNSs in which the size was controlled by changing the ratio between the Au precursor and the amount of Au−Fe_3O_4 seeds. Two groups of nanoparticles were formed in this way, the first one named big JNSs: A.1, B.1, C.1, with sizes between 57 and 75 nm and a plasmonic band close to the laser used in the photothermia, and one named small JNSs: A.2, B.2, C.2, with sizes between 26 and 34 nm, showing only a shoulder in the tips-related plasmonic band. Specific details of the synthesis parameters of these NPs can be found in Table S2.

Synthesis of Sphere-Shape Au−Fe_3O_4: JNSphs. 10 g of PVP was initially dissolved in 200 mL of DMF. Immediately after that, 1.092 mL of $HAuCl_4{\cdot}3H_2O$ (50 mM) was added to the solution and stirred for 6 min. Then, a certain volume of Au−Fe_3O_4 seeds was added (identical to the one used for the small JNSs) to obtain JNSphs named A.3, B.3, and D.3. Synthesis conditions can be found in Table S2. Once added, the reaction flask containing the mixture was placed in an oil bath at 120 °C and stirred for 1 h until a bright red solution was obtained. The flask was then taken out and left until it cooled down.

JNSs and JNSphs Purifying Procedure. The solution containing the Au−Fe_3O_4 Janus NPs was cleaned using ethanol by 3−4 centrifugation cycles at 6000−9000 rpm for 1 h. The final precipitate was redispersed in 1−2 mL of Milli-Q water and stored in the fridge.

PMAD-Functionalized JNPs: Transfer of Au−Fe_3O_4 Heterodimers to Water. Dodecyl-functionalized poly(maleic acid) (PMAD) was synthesized according to a previous report,[43] by reacting poly(isobutylene-*alt*-maleic anhydride) (M_W = 6000 g mol^{-1}, Aldrich) with dodecylamine (75% with respect to PMA monomers). A solution of heterodimers in chloroform was placed in a glass vial; 100, 350, and 150 μL of A, B, and C with (Au/Fe_3O_4 concentration: 7.5, 0.74, and 1.5 mg/mL). PMAD polymer solution in chloroform (0.08 M and 233, 36, and 25 μL, respectively) was added followed by shaking at room temperature for 30 min. The added PMAD volume was calculated according to the concentration of NPs (obtained by drying part of the solution) to have approximately 100 monomer units for each nm^2 nanoparticle surface. The solvent was completely evaporated via a rotatory evaporator and then the dried solution was dissolved in an aqueous solution of sodium hydroxide (1 mL, 0.1 M) and sonicated in an ultrasound bath. The solution was then centrifuged one time (12×10^3 rpm, 30 min) to remove the residual polymer and redispersed in 1 mL of Milli-Q water.

Etching of the Au Domain from Au−Fe_3O_4 Heterodimers. Etching of Au−Fe_3O_4 heterodimers with Lugol's solution was performed on PMA-functionalized JNPs. Strong oxidation of gold with Lugol's solution ([I_2 concentration: 2% (w/v)] and [KI concentration: 4% (w/v)]) was used to etch the gold domain in the heterodimers as previously reported.[34] 17 mL of a 50 times diluted Lugol's solution was mixed with 150 μL of heterodimers in water (Au concentration: 2.24 μM).

The solution was heated to 60 °C for 1 h. Afterward, the solution mixture was lightly sonicated, and 2 centrifugation cycles were carried out with Milli-Q water.

Transmission Electron Microscopy. All NPs were characterized using transmission electron microscopy (TEM). Samples of JNPs were fixed on 400 square mesh Cu grids with a carbon coating by depositing a drop of solution and letting it dry. TEM images were obtained by using JEM-1400 PLUS JEOL equipment working at 100 kV. ImageJ software program was used to obtain the relative sizes of the nanoparticle components.

UV−Vis−NIR Spectroscopy. The absorbance of JNPs was measured via UV−vis spectroscopy (Cary 60, Agilent) between spectral ranges of 350−1100 nm using diluted aqueous solutions in a standard cuvette. Au concentrations for JNSs and JNSphs were calculated by assuming an absorbance of 1.2 for 0.5 mM at 400 nm.

X-ray Diffraction. Diffractograms were collected using a Philips X'pert PRO automatic diffractometer operating at 40 kV and 40 mA, in a theta−theta configuration, a secondary monochromator with Cu Kα radiation (λ = 1.5418 Å), and a PIXcel solid-state detector (active length in 2θ 3.347°).

The samples were mounted on an Eulerian cradle with an automatically controlled $X-Y-Z$ stage. The diffractograms corresponding to heterodimers and NSPhs can be seen in Figure S1 where the peaks fit well to magnetite and metallic Au.

Vibrating Sample Magnetometer. Magnetic hysteresis loops were assessed by a vibrating sample magnetometer (VSM, MicroSense EZ7) with a sensitivity of 5×10^{-6} emu, up to a maximum applied magnetic field of 18 kOe at room temperature.

AC Magnetometry. Measurements of the SAR [specific absorption rate, a.k.a. specific loss powers (SLP)] were obtained using AC magnetometry in a homemade instrument that produced a strong magnetic field capable of saturating the samples as previously reported.[44] This instrument can operate in a broad frequency range with high field strengths. At room temperature, the dynamic hysteresis loops were measured at various frequencies of 143, 350, and 732 kHz.

The magnetometric measurements were made using JNPs dispersed in Milli-Q water, which was introduced in a plastic capsule and inserted in the instrument. Using the hysteresis loops, the SAR was calculated by the loop areas and the applied frequency according to the formula[45]

$$\mathrm{SAR} = \frac{f}{c}\mu 0 \oint M \mathrm{d}H \tag{1}$$

where f is the frequency, c the concentration, M the magnetization, and H is the applied magnetic field. The sample mass was calculated using a VSM and assuming a constant magnetization of saturation, which is true for nanoparticles big enough, with negligible contribution from surface atoms.

https://doi.org/10.1021/acsanm.3c03818
ACS Appl. Nano Mater. 2023, 6, 18466−18479

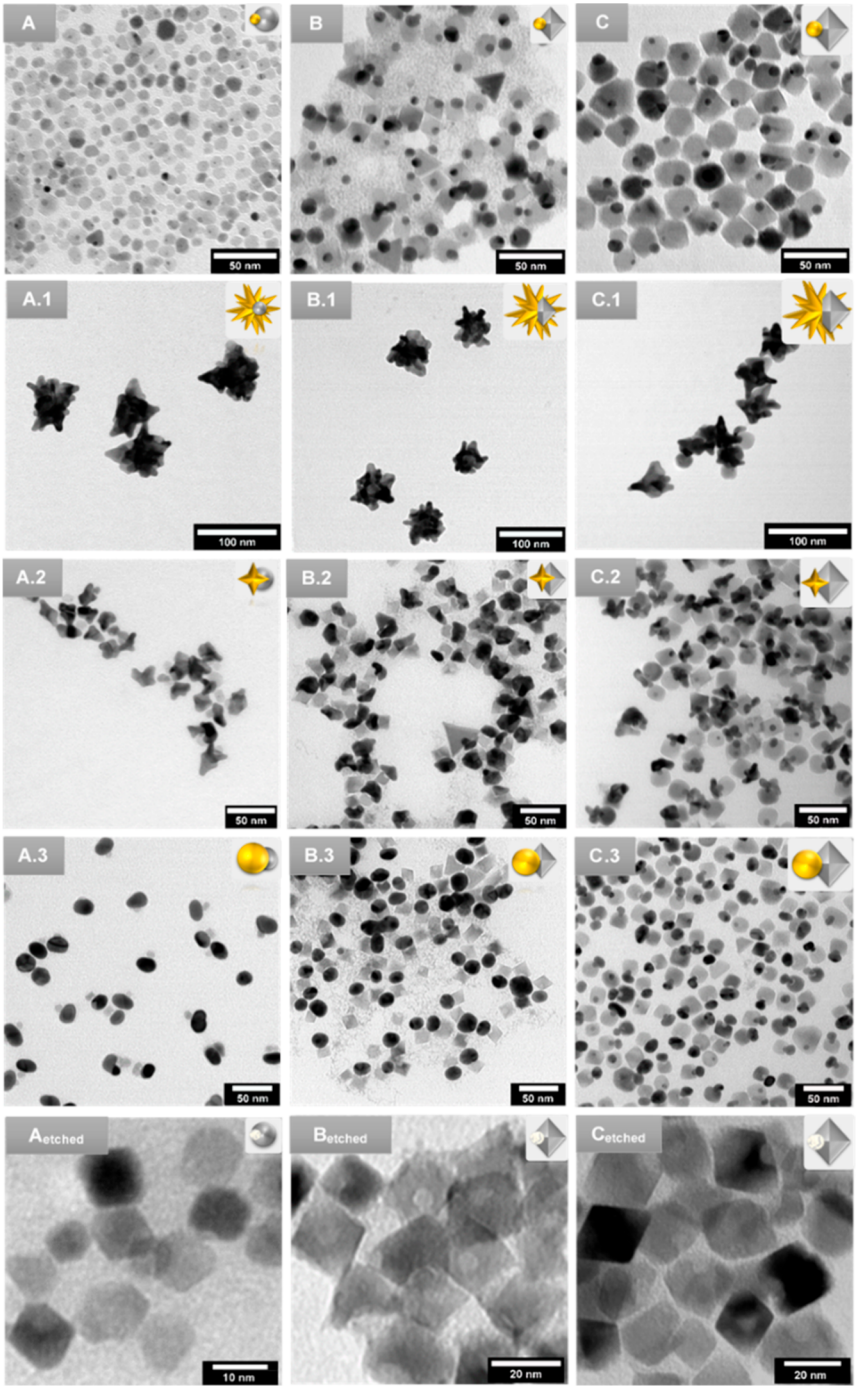

Figure 1. (A–C) TEM images of synthesized JNPs with three different sizes of the Fe_3O_4 component from 10 to 30 nm of iron oxide and different morphologies and sizes of the Au component, JNSs (A.1–C.1), and (A.2–C.2)from 20 to 70 nm , and JNSphs (A.3–C.3) from 17 to 25 nm . A_{etched}–C_{etched} correspond to Fe_3O_4 NPs after etching the Au components of the related heterodimers.

The NPs were also compared under the biological safety limits of magnetothermia, It is usually considered that this limitation can be mathematically expressed by the criterion $H \times f \leq L$. The calculation of the SAR_{limit} takes into account that the magnetic field amplitude and the frequency of the applied electromagnetic excitation must fit within certain medically safe conditions. For instance, under the widely accepted Hergt's criterion, this number, L, is set to 5×10^9 Am^{-1} s^{-1}. Note here that several limits, lower and higher, have been proposed in the literature, and it is a topic of scientific debate.[46−48] If SAR results from the product of the hysteresis loop area by the frequency of the driven field, then the calculation of the SAR_{limit} for a given field amplitude H is just the product of SAR/f by the limiting frequency $f_{limit} = L/H$. However, this is generally not true because the hysteresis loop area can also depend, in turn, on the frequency. In general, the SAR_{limit} determination demands obtaining several SAR(H) curves at different frequencies that should be conveniently spaced out in order to get a reliable analytical SAR(H,f) function. This function allows fitting the existing experimental data, and it is expected to work only for a given sample and in the range of frequencies between minimum (143 kHz in this work) and maximum (732 kHz). In our case, we have used the following sigmoidal function as previously described[49]

https://doi.org/10.1021/acsanm.3c03818
ACS Appl. Nano Mater. 2023, 6, 18466−18479

$$\mathrm{SAR}(H,f) = p^1(f) + \frac{p^2(f)}{1 + e^{-(\mu_0 H - p^3(f))/p^4(f))}} \quad (2)$$

where a set of parameters (p^1, p^2, p^3, p^4) are fitted to any experimental SAR(H) curve. Once the fittings of all SAR(H) curves are done, the best-obtained parameters are fitted in turn to a polynomial function (up to the second degree) of the frequency f

$$p^n = c_0^n + c_1^n \cdot f + c_2^n \cdot f^2 \quad (3)$$

where n = 1, 2, 3, 4.

When the polynomial functions given by (3) are inserted in eq 2, a function of two variables (H,f) is obtained, which can be used to calculate the SAR of a given sample for whatever excitation conditions. (An example of the fitting can be seen in Figure S2).

Photothermal Measurements. A 785 nm laser (Lumics, LuOcean Mini4) connected to a reflector collimator (Thorlabs) was used to have a collimated beam of approximately 12 mm. The light passed through a 1 × 1 cm^2 mask placed in front of a standard UV−vis PS cuvette (1 cm^2 section) containing 1 mL of the NP sample at a concentration of Au of 0.1 mM. In addition, a thermal power meter (S425 Thorlabs) was placed behind the sample to measure the light power before and after placing the sample. An illumination power of 0.3 W cm^{-2} was applied as a biological safety value to induce the photothermal effect of the NP solution. On−off experiments (20 + 30 min) as well as transmittance experiments (regression line at different laser powers) were performed.[50] 20 min was chosen as a compromise time to avoid evaporation of the sample (note here that this could give a slight underestimation of the conversion efficiency) and reach a temperature saturation. An infrared thermal imaging camera (Flir E4) placed on top of the cuvette was used to monitor the temperature and assess the temperature by using the Flir tools + software.

To obtain the SAR, the thermograms were analyzed using a modification of the corrected-loss method described by Wildeboer et al.[51] Assuming a linear loss regime, the losses were calculated from the cooling part and subtracted to the thermogram (a step-by-step description of the protocol is included in the Supporting Information, figure S3). The SAR was obtained using the corrected thermogram as

$$\mathrm{SAR} = \frac{c}{m_{\mathrm{NP}}}\left[\frac{\mathrm{d}T}{\mathrm{d}t_c}\frac{\mathrm{d}T}{\mathrm{d}t_{c,\mathrm{water}}}\right] \quad (4)$$

where C is the heat capacity of the sample ($C = m_{\mathrm{water}} c_{\mathrm{water}}$), m_{NP} is the mass of NPs, and the derivatives of the temperature are taken in the corrected-losses thermograms.

The photothermal conversion efficiency (η) can also be obtained from the corrected-losses thermogram as

$$\eta = C\frac{\left[\frac{\mathrm{d}T}{\mathrm{d}t_c} - \frac{\mathrm{d}T}{\mathrm{d}t_{c,\mathrm{water}}}\right]}{I_o(1 - T_r)} \quad (5)$$

where I_0 is the incoming power after subtracting the cuvette and water absorbance, and T_r is the transmittance of the sample at the illumination wavelength.

RESULTS AND DISCUSSION

Synthesis and Structural Control. To generate a library of JNPs with different sizes and shapes, heterodimers of Au:Fe_3O_4 were initially synthesized. These heterodimers were obtained by modifying different protocols,[41,42] which involve a one-pot two-step synthesis and can offer tunability on the size of the Fe_3O_4 component (see Experimental part). The two steps involve the generation of Au NPs at intermediate temperatures (120−150 °C) and then a temperature ramp to the boiling point of the solvent, where the Fe grows on one side of the Au NPs that act as seeds. While it could be expected that by changing the ratio of iron pentacarbonyl to Au, different sizes could be obtained, we observed that this approach offers size tunability only when small changes in iron pentacarbonyl are used. When the ratio is highly modified, like in this case, this is not true due to the appearance of homogeneous nucleation giving rise to homocomponent Au or Fe_3O_4 NPs. This can be solved by adjusting the synthesis parameters, such as the temperature profile or the added ligands, to obtain the heterodimers. Scheme 1 illustrates the diagram of the Au:Fe_3O_4 JNP synthesis with structural control through (A) changing the size of the Fe_3O_4 component of JNPs via variations in the thermal decomposition method followed by (B) growing the Au component for different sizes and shapes by a seed-mediated-growth synthesis.

For standard initial conditions (see Experimental Section), Au:Fe_3O_4 heterodimers were formed with gold and iron oxide domains, having average diameters of Au as 2.6 and Fe_3O_4 as 10.8 nm. For bigger sizes, we started the reaction with the surfactant mixture without adding HDD (similar to the protocol by Pellegrino et al.[41]) and changing the holding time and annealing temperature as described in Table S1, which gave sizes of Fe_3O_4 as 24.0 and Au as 10.88 ± 2.44 nm. Finally, bigger sizes were obtained by increasing the holding time at 200 and 300 °C for 30 min more, which gave an Fe_3O_4 size of 30.6 nm and a Au size of 7.2 nm. As can be seen in the TEM images (Figure 1A−C), while NPs with small Fe_3O_4 tend to show a spherical shape, for bigger sizes, there is a high abundance of polyhedral shapes. These shapes are indicative of single-crystal NPs and have been shown to present a good capacity for magnetic hyperthermia.[17,52]

The obtained heterodimers show the Au component as the smallest part of the NP (Figure 1A−C), which gives rise to a poor and broad plasmonic band hindered by the metal oxide component (Figure S4).[53] In addition, the NPs are coated with apolar ligands, and therefore, they are not water-soluble. These two drawbacks can be solved by growing the Au part as a nanostar, using a seed-mediated-growth method in the presence of PVP which acts as a shape-directing and water-stabilizing agent, as it has been previously described.[37,39] In this synthesis, the size of the Au part can be perfectly tuned by changing the ratio between the reaction Au and the seeds, as the reaction has a nearly 100% yield and no homogeneous nucleation takes place. We selected two nanostar sizes for each heterodimer: one with a plasmonic band close to the laser wavelength and one smaller, at the limit of the nanostars formation, with a plasmon band blue-shifted with respect to the laser wavelength. The TEM images in Figure 1 (A.1, B.1, and C.1) show the produced large JNSs with an average diameter of 55−75 nm and the small JNSs of 25−35 nm Figure 1 (A.2, B.2, and C.2).

To determine the relevance of the shape of the Au component for both photothermia and magnetothermia, we developed the synthesis of PVP-coated sphere−sphere NPs (JNSphs) by a modification of the JNSs synthesis. By increasing the temperature of the synthesis reaction to 120 °C during the growing process, two competitive processes take place. One is the formation of tips induced by PVP, and the other one is a temperature-induced reshaping process that tends to form spherical morphologies.[54] The reaction can change colors between red, purple, and blueish depending on the reaction volume and therefore on the time needed to reach the setup temperature. However, after waiting long enough, it always ends up being red, indicative of a structure with spherical Au shapes. In this case, for comparison reasons, the

https://doi.org/10.1021/acsanm.3c03818
ACS Appl. Nano Mater. 2023, 6, 18466−18479

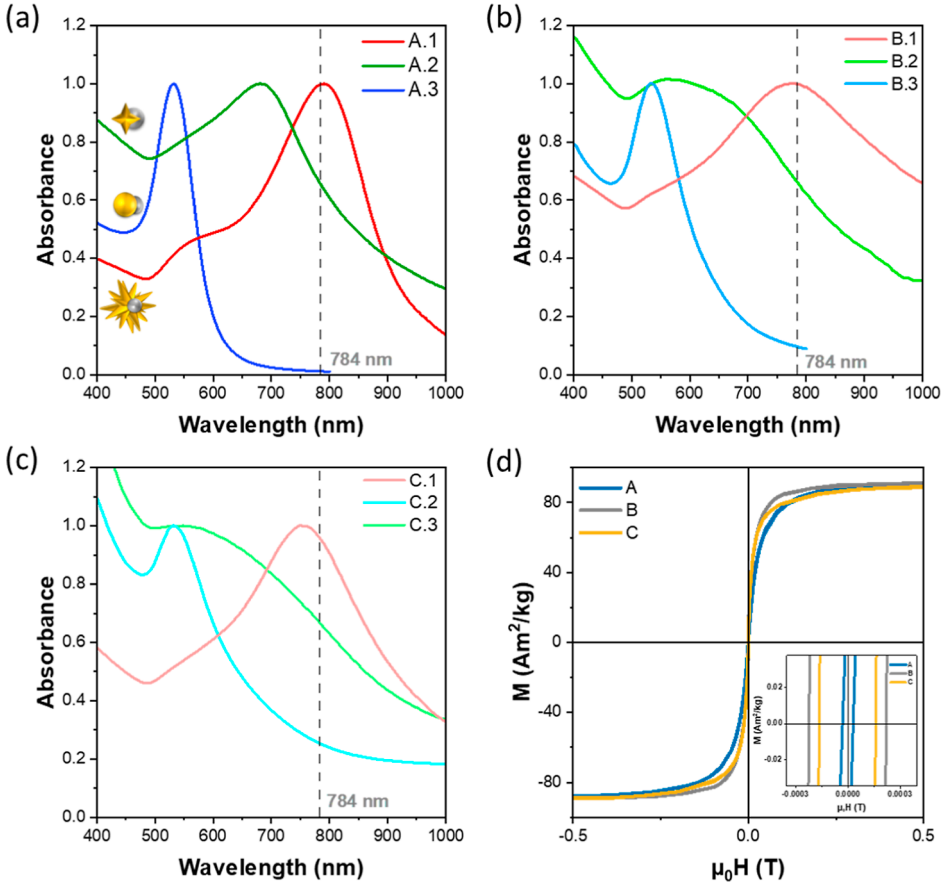

Figure 2. Optical and magnetic characterization of the obtained Janus nanoparticles. (a–c) UV–vis–NIR absorbance spectra of different shapes and sizes of the Au component of JNPs at different sizes of iron oxide used as seeds. Letters, A–C, indicate the Fe_3O_4 size and numbers to the type (1) big JNSs; (2) small JNSs; and (3) JNSphs. (d) VSM magnetic hysteresis loops (M–H) of heterodimers with different sizes of the Fe_3O_4 component (A–C) normalized to the amount of Fe. The inset displays an enlarged image close to the zero magnetic fields. (A) [Fe_3O_4]: 10.8 nm, (B) [Fe_3O_4]: 24.0 nm, (C) [Fe_3O_4]: 30.6 nm.

Table 1. Optical Characteristics of all Designed JNPs (JNSs and JNSphs)[a]

sample	λ_{max} (nm)	λ_{max}—Gaussian fitting (nm)		ε_{785nm} (M^{-1} cm^{-1})	η (%)	ΔT_{max} (°C)	SAR (kW/g)
		peak 1	peak 2				
A.1	791	605	794	7053	44.3 ± 4.5	12.0	2.48
A.2	680	577	694	1890	22.2 ± 4.2	6.2	1.87
A.3	534			53.79	10.2 ± 5.7	1.5	0.019
B.1	778	553	770	3502	49.5 ± 13.6	8.8	2.54
B.2	561	577	704	1382	25.9 ± 6.1	3.6	0.86
B.3	534			290.4	24.3 ± 8.5	2.3	0.23
C.1	751	591	756	3918	50.0 ± 12.7	9.3	2.36
C.2	535	561	761	1138	32.8 ± 3.5	4.1	1.54
C.3	532			561.8	11.4 ± 4.4	2.1	0.28

[a] λ_{max} corresponds to the wavelength at maximum absorbance (nm); in the Gaussian fitting, the wavelength is given for the maximum absorbance of the two main plasmonic modes; $\varepsilon_{785\ nm}$ corresponds to the molar extinction coefficient; η (%) is the conversion efficiency, ΔT_{max} and SAR are the maximum temperature achieved in photothermia and SAR (785 nm, 0.3 W cm^{-2}, 0.1 mM).

synthesized JNSphs were obtained with the same component ratios as the JNSs (fixing the amount of seed solution added to a given growth solution). Although both sets of NPs should have the same volume size, the TEM images of the JNSphs, Figure 1 (A.3, B.3, C.3), show sizes of 18–27 nm, slightly smaller than the corresponding JNSs, as a consequence of using the equivalent diameter for its evaluation (obtained from the area of the 2D projection of the TEM images and assuming a spherical shape) (see Table S2).

Finally, Fe_3O_4 NPs with the exact same size and shape as those of the rest of the NPs were obtained by etching the gold component of the initial heterodimers. For that, the heterodimers were transferred to water using a micellar coating strategy with the amphiphilic polymer PMAD, which allowed having all samples in the same solvent for their characterization. Once transferred to water, the NPs were exposed to an aqueous mixture of I_2 and KI_3 (Lugol's solution) for the Au etching. As observed in the TEM images (Figure 1,A_{etched}–

https://doi.org/10.1021/acsanm.3c03818
ACS Appl. Nano Mater. 2023, 6, 18466–18479

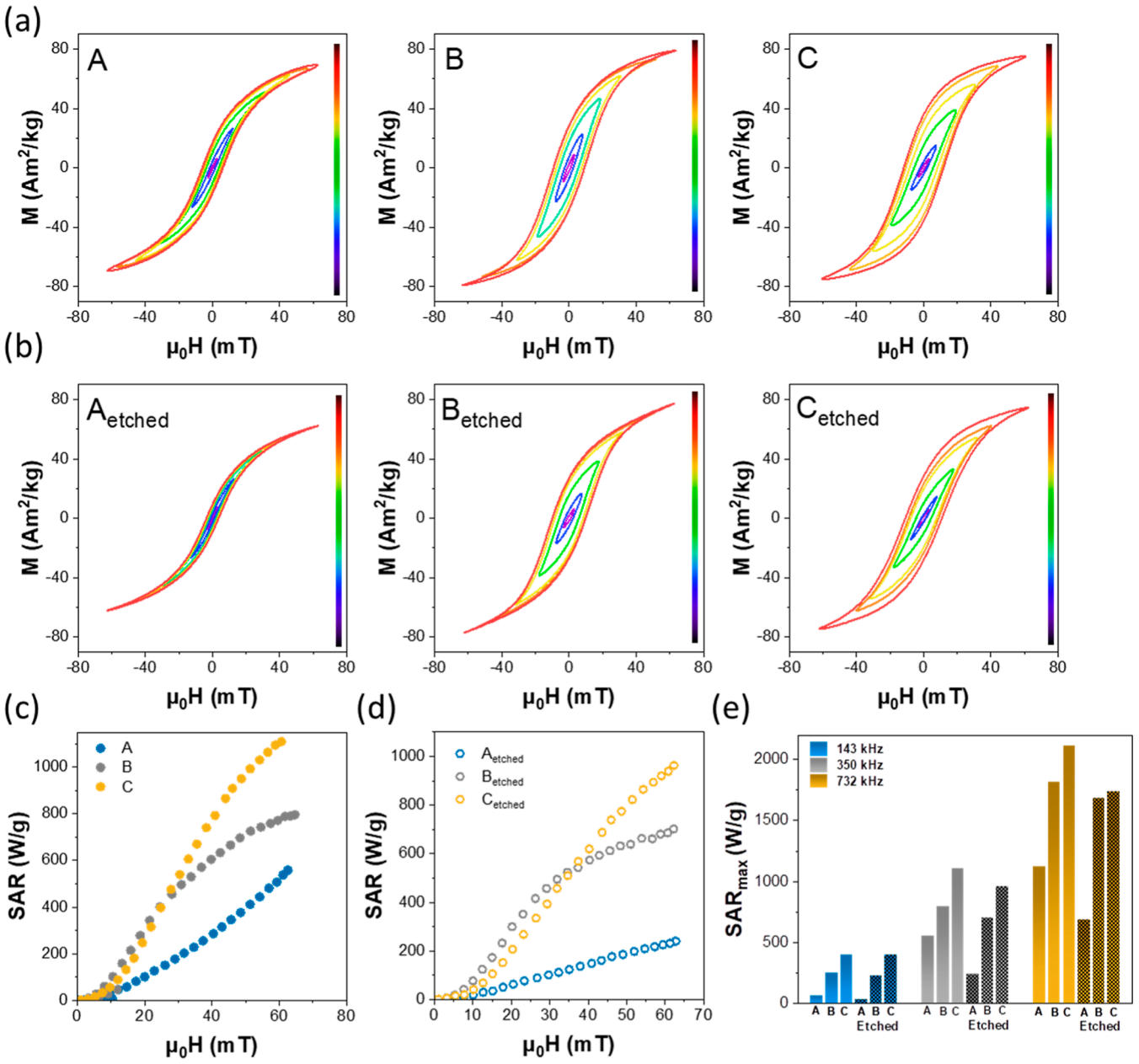

Figure 3. (a,b) M−H loops of Au−Fe_3O_4 Janus NPs before and after etching the Au component (at 350 kHz at 20 °C). (c,d) SAR as a function of the applied magnetic field (0−80 mT) of Au−Fe_3O_4 heterodimers before and after Au etching (350 kHz at 20 °C). (e) Maximum SAR of all heterodimers with and without etching at three different frequencies (143, 350, and 732 kHz).

C_{etched}) the Fe_3O_4 NPs show similar shapes but contain a small cavity where the Au was placed.

Physical Characterization. *Optical Properties.* The LSPR dipolar mode of the JNSphs (Figure 2a−c) takes place around 534 nm, which is slightly higher than for spherical Au NPs of the same size,[55] due to the effect of the refractive index of the Fe_3O_4 component. For JNSs, two hybrid dipolar plasmonic bands appear: one related to the tips of the NSs at longer wavelength and one related to the body of the NPs at shorter wavelengths.[56]

The position of the tips' plasmonic mode red-shifts with the tips' aspect ratios and therefore with the size of the nanostars. For the large JNSs (A.1, B.1, and C.1), this takes place at the near-infrared region with wavelengths close to 785 nm (illumination laser for photothermia) (Table 1). On the other hand, a small shoulder is observed at around 550−600 nm, corresponding to the body plasmonic mode. For small JNSs (A.2, B.2, and C.2), which present shorter tips, the plasmonic band is presented at much shorter wavelengths. Despite this blueshift with respect to big JNSs, they still show a relatively high absorbance at 785 nm, definitely much higher than the corresponding JNSphs. The deconvolution in peak 1 and peak 2 shows the two main peaks, with peak 2 of A1, B1, and C1 being close to the excitation wavelength and slightly lower wavelengths for the cases of A2, B2, and C2 (except C2 which was difficult to fit at these wavelengths). For peak 1, on the other hand, a better fitting was obtained for A2, B2 and C2. In any case, all values were obtained in the same interval (553−605 nm).

Magnetic Properties. The magnetic characterization of the obtained NPs was performed by conventional vibrating-sample magnetometry (Figure 2d). The room-temperature magnetic

https://doi.org/10.1021/acsanm.3c03818
ACS Appl. Nano Mater. 2023, 6, 18466−18479

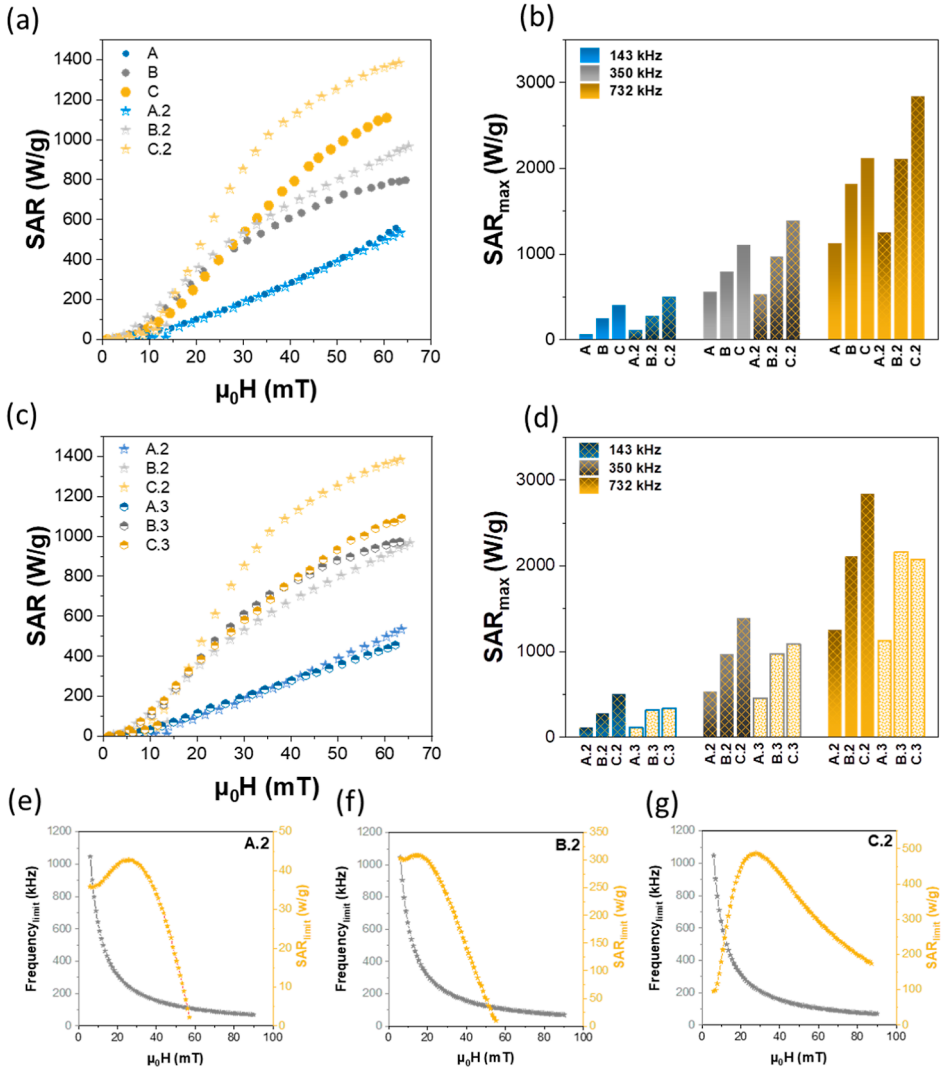

Figure 4. (a) SAR values at 350 kHz as a function of the magnetic field in the range [0−80 mT] of Au−Fe_3O_4 heterodimers and JNSs with different sizes of the iron oxide domain (from 10 to 30 nm). (b) Comparative SAR_{max} values at three different frequencies [143, 350, 732 kHz] of Au−Fe_3O_4 heterodimers and JNSs. (c) SAR values at 350 kHz as a function of the magnetic field in the range [0−80 mT] of Au−Fe_3O_4 JNSs and JNSphs. (d) Comparative SAR_{max} values at three different frequencies [143, 350, 732] kHz of Au−Fe_3O_4 JNSs and JNSph. (e−g) Maximum attainable SAR_{limit} under the biological safety conditions of A.2, B.2, and C.2 samples. The black curve represents the appropriate maximum frequency, $H \times f = 5 \times 10^9$ A m^{-1} s^{-1}, for a given magnetic field intensity and the yellow is the corresponding SAR_{limit} at that frequency.

hysteresis loops for a range of Au−Fe_3O_4 heterodimer sizes displayed a low coercivity (μ_0Hc), below 0.3 mT, both as a heterodimer and as a homocomponent after Au removal (Figure S5). Both saturation magnetization and the hysteresis loops are not significantly different among samples. This behavior was maintained for all samples independently of the Au component.

Hyperthermia Properties. *Magnetic Hyperthermia.* Due to the different dimensions of the iron oxide components of the three different sets of NPs, it is expected that they also exhibit significantly different magnetothermal features. To evaluate it, AC magnetometry was used instead of conventional thermometry. AC magnetometry offers the possibility to measure a wide set of conditions in a short time while giving reliable results obtained directly from the integration of the hysteresis loop.[57−59] The SAR obtained by this integration accounts for the different mechanisms of magnetothermia, including Neel and Brown relaxations.[60] In addition, it is expected to avoid possible errors obtained in the measurements or analysis of the calorimetric data (temperature gradients or too simplistic models).[51] Despite this, when the tests are well performed, they have been shown to offer similar results.[61]

The magnetothermal capabilities of iron oxide heterodimers of the three different dimensions of Fe_3O_4 were initially assessed. At first sight, significant differences are observed in the shape of AC hysteresis loops when comparing the three different sizes, A, B, and C, at 350 kHz and 20 °C (Figure 3a). Sample A displays the narrowest hysteresis loop, which grows to a more squared shape as the NPs get bigger from A to C. The magnetothermal capabilities of heterodimers were compared with those of NPs of Fe_3O_4 with the same size for this component. For that, the Au in the heterodimers was previously etched. Note here that removing the Au from the initial heterodimers instead of synthesizing Fe_3O_4 NPs with similar sizes guarantees the exact same size and size distribution of the Fe_3O_4 component of the heterodimers, including the little indentation where the Au was located

https://doi.org/10.1021/acsanm.3c03818
ACS Appl. Nano Mater. 2023, 6, 18466−18479

(Figure 1). Interestingly, the shapes of the loops change after the etching of the Au component (Figure 3b). For instance, after etching the Au component from sample A, it shows a much narrower hysteresis loop. This difference is less significant for the cases of samples B and C, where only a minimum effect is observed. The same observation was noticed in the M−H loops values at lower and higher frequencies (143 and 732 kHz, Figures S6 and S7, respectively). The magnetic SAR was extracted, according to formula 1, from the mentioned hysteresis loops as a function of the magnetic field for the three iron oxide diameters before and after etching the Au component (Figure 3c,d). The results at 350 kHz show the typical monotonous increase in the SAR with the magnetic field. The smallest NPs, sample A, show the lowest values of SAR, while for the other samples, the effect of size is appreciable only at a high magnetic field above ∼30 mT. The same behavior was observed for lower and higher frequencies, 143 and 732 kHz, respectively (Figure S6c,d and S7c,d). When the samples before and after etching are compared, a general increase in SAR is observed for all conditions (Figure S8). This can be easily observed in Figure 3e, which represents the SAR at the highest magnetic field of our instrument, i.e., SAR_{max}, for all heterodimers before and after etching at the three frequencies. In this case, the bigger the Fe_3O_4 component, the bigger the SAR_{max}. This SAR dependency on the size may differ from what has been found in other works with magnetite NPs, where the SAR grows only up to a certain NP size and then decreases. The size of NPs at which the maximum of SAR appears is not clear in the literature, as it depends on the synthesis type and on the magnetothermia conditions applied.[62−64] In our case, the results indicate that at 30 nm, we are still below that threshold for large magnetic fields. On the other side, at lower magnetic fields below 30 mT, the NPs showing the highest SAR correspond to the intermediate size, in line with the previous results (Figure 3). Finally, the presence of Au in the heterodimers produces a slight increase in the SAR for all cases, probably due to a higher colloidal stability of the Au-containing NPs.

Similar AC-magnetometry experiments were performed for the NPs after growing the Au component with the two possible Au shapes (set 2 for JNSs and set 3 for JNSphs). In general, the NPs with larger Au content (A.2−C.2 and A.3−C.3) showed higher SAR values compared to the heterodimers and the magnetic NPs alone, as can be seen in Figure 4a,c for the 350 kHz. These higher values of SAR were also found for lower and higher frequencies (Figures S9 and S10) and in the summary of SAR_{max} in Figure 4b−d, following the same tendency observed above for the heterodimers with and without etching, i.e., the growth of the Au component tends to increase the SAR and therefore the magnetothermal capabilities of the multicomponent Au:Fe_3O_4 NPs. Note here that the Au component does not contribute to the magnetic properties. Although the effect is not completely understood, this could be due to an increase in dipolar decoupling, similar to what has been observed for core@shell NPs.[24,65] At the high concentrations used in the experiments, of around 1 mg mL^{-1}, some aggregation could take place. The Au component could help to stabilize the NPs or act as a spacer for the case of the aggregated or agglomerated NPs, improving the decoupling among the Fe_3O_4 nanoparticle lobes and therefore improving the SAR. The higher Au quantity from etched to heterodimers and finally to JNSs and JNSphs produces a monotonous increase in the SAR.

When comparing the different shapes, i.e., JNSs and JNSphs, less clear differences have been observed (Figure 4c−d). For instance, at 350 kHz, JNSs showed higher SAR values than JNSphs for sample C, while for samples B and C, the values were almost identical (slightly higher for A and lower for B). For 143 and 732 kHz (Figures S6, S7, and 4b), JNSs also showed higher values of SAR than JNSphs for sample C. For samples A and B, JNSs show almost the same behavior as the JNSphs at 732 kHz and relatively higher for JNSphs at 143 kHz.

Regarding the effect of the frequency, SAR/f can be obtained directly from the integration of the hysteresis loops according to formula 1. In general, for the frequencies used here, higher frequencies generated a higher SAR/f (Figure S11), which tends to be more evident in higher magnetic fields. Here, it is important to consider the limitation of using magnetothermia in healthy tissue, which limits the value of $H \times f$ applied to the patient.[66−68] Several biological safety limits have been proposed in the literature, which depend on many factors such as preclinical or clinical application, the method of evaluation (biochemical or discomfort feeling), the size of the coil, or the region or type of tissue where they have been applied.[46−48] These limits go from low values like the one found by Atkinson, 4.8×10^8 A m^{-1} s^{-1} for the thorax,[69] or the 6, 7.5, and 13.5×10^8 A m^{-1} s^{-1} found for the thorax, neck, and head/brain of humans (both based on discomfort),[70] and the high-value limits like the 9.5×10^9 A m^{-1} s^{-1} found on biochemical preclinical assays.[67] Here, we have used the Hergt's limit, $H \times f \leq 5 \times 10^9$ A m^{-1} s^{-1}, as an intermediate limit and highly used in the literature.[46−48] To perform this analysis, we have empirically fitted the obtained results as a function of the frequency and magnetic field using formula 2 described in the Experimental Section. Figure 4 represents this limit at different magnetic fields and the corresponding frequency for the three JNSs with varying Fe_3O_4 lobe sizes. A maximum SAR_{limit} is observed for all NPs (Figure S12). The maximum values occur between 14 and 28 mT and 110 and 429 kHz, depending on the sample (Table 2), and reaching the highest value at 486 W g^{-1} for samples C.2 but also high values, above 300 W g^{-1}, for NPs with medium and big Fe_3O_4 lobe sizes and both shapes JNSs and JNSphs. These values are in line with what has been in the literature for efficient NPs like nanoflowers or highly crystalline nanoparticles[52,71] (between 400 and 700) and not too far from the best Fe_3O_4 NPs like the

Table 2. Values of H, f, and SAR Obtained From the Empirical Fitting of SAR (f, H) and the Biological Safety Constraints, $H \times f = 5 \times 10^9$ A m^{-1} s^{-1}

sample	optimal $(H \times f)_{limit}$ (mT kHz)	maximum$SAR_{limit-max}$ (W/g)
A	28 × 219	196
A.2	27 × 232	243
A.3	19 × 339	140
A_{etched}	14 × 429	77
B	15 × 110	297
B.2	17 × 374	309
B.3	26 × 232	340
B_{etched}	24 × 259	258
C	23 × 263	273
C.2	27 × 231	486
C.3	21 × 297	348
C_{etched}	28 × 216	252

https://doi.org/10.1021/acsanm.3c03818
ACS Appl. Nano Mater. 2023, 6, 18466−18479

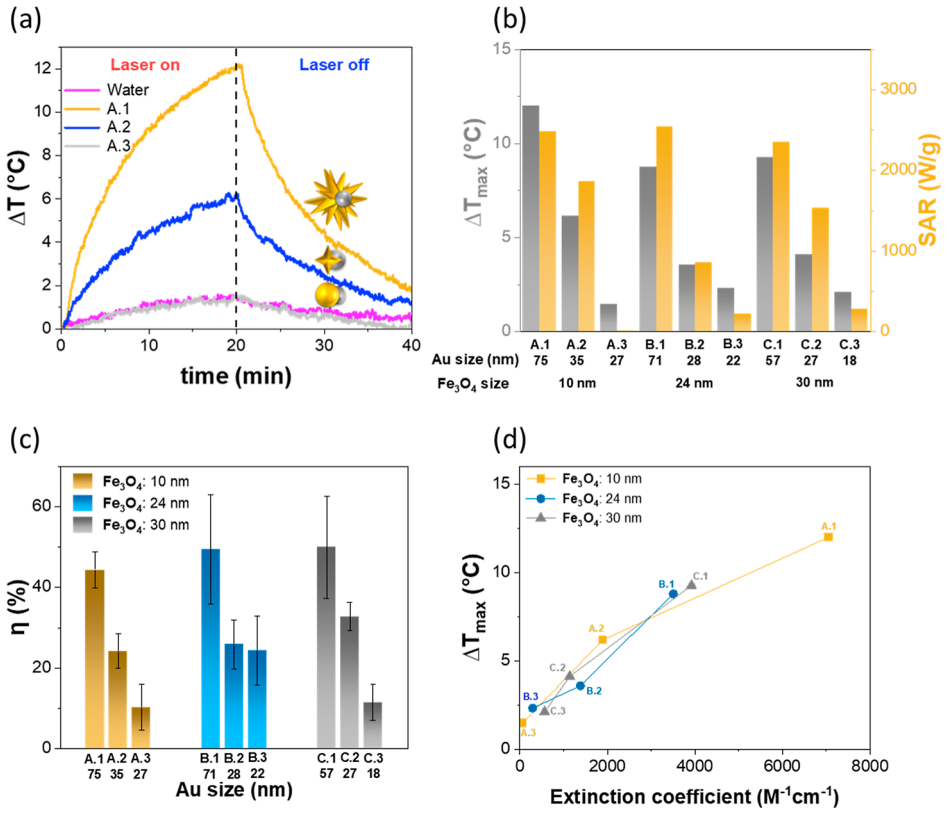

Figure 5. (a) Thermogram in an on−off experiment under NIR-laser irradiation of JNPs with the same size of the Fe_3O_4 component and different sizes and shapes of the Au component (A.1, A.2, and A.3) and fixed illumination conditions (1 mL, 0.1 mM of Au, 785 nm, and 0.3 W cm^{-2}). (b) Maximum temperature increment and SARs for the tested Janus NPs. (c) Photothermal conversion efficiency (η) for the different JNSs and JNSphs. (d) Maximum temperature variation as a function of the molar extinction coefficient.

ones of magnetosomes or the truncated octahedra NPs, which are around 1 kW g^{-1}.[49,71] Note here that this value is highly dependent on the safety limit considered. For instance, when 9.5×10^9 A m^{-1} s^{-1} is considered instead of Hergt's limit, a $SAR_{limit\text{-}max}$ close to 1kW g^{-1} is obtained for sample C2.

Overall, the presence of the Au component appears to be efficient for improving the SAR, which allows the use of a lower concentration of NPs or lower magnetic fields for magnetothermal applications at diverse frequencies, particularly for the NPs with large sizes of the Fe_3O_4 component. Additionally, the shape of the gold component does not seem to have a clear effect on the magnetothermal effect in the SAR_{max}, except for sample C, where the nanostar shape seems to improve the SAR_{max}.[8] As mentioned above, the Au component should not contribute to the magnetic properties; therefore, this effect could be related to a separation mechanism in aggregation induced by concentration and a decoupling effect among the Fe_3O_4 lobes. From that point of view, the JNSs could act as slightly better spacers due to a more steric separation. Finally, considering $H \times f$ biological safety constraints for the use of magnetothermia, increasing the Au component has a beneficial effect but the highest values are also obtained for the biggest Fe_3O_4 lobe size and high Au content.

Plasmonic Photothermia. The same Au−Fe_3O_4 JNSs and JNSphs were evaluated for photothermal applications. In this case, given the significantly superior efficiency of plasmonic photothermia with respect to magnetothermia, a lower concentration of 0.1 mM Au was used. Regarding the excitation wavelength, the first transparency window takes place in the range ∼650−950 nm,[72] being the lower limit due to proteins such as hemoglobin and the upper one due to the first band of the IR water absorption. Thus, we selected an intermediate value of 785 nm, which is in the middle of the first transparency region and a typical laser wavelength. On the other hand, a low power density of 0.3 W cm^{-2} of illumination was chosen to be below the safety limit to avoid any damage to healthy tissue.[73−75]

The JNPs exhibited remarkable photothermal efficiency, even at this low concentration and power. For instance, sample A.1 reached a temperature increase close to 12 °C after 20 min of illumination (Figure 5a). Under similar conditions, the small JNPs (A.2), in which the LSPR takes place at much lower wavelengths, reached an increase of temperature of 6 °C, enough to cause cell apoptosis.[68] When compared with the JNSphs (A.3), which show a plasmonic band around 540 nm, no absorption appears at 785 nm, therefore no increase in temperature is detected with respect to the water control. It is worth noting that although Fe_3O_4 NPs could have absorption of light at the NIR and therefore photothermal effect, the required concentration to cause a measurable increase in temperature is much higher than the one used here.[8,24]

When the ΔT_{max} and SAR for all samples are compared (Figure 5b), both parameters show similar trends. In all sets of JNPs, the best results were achieved for the large JNSs, followed by the small JNSs, and finally the JNSphs (Figure 5b). In these cases, the effect of the size of iron oxide was minimal, with a slightly better performance of the NPs with smaller iron oxide lobes. The SAR values were in the kW g^{-1} order of magnitude without the need to use high powers. For the best

https://doi.org/10.1021/acsanm.3c03818
ACS Appl. Nano Mater. 2023, 6, 18466−18479

case, the A1 and B1, the SAR was 2.5 kW g^{-1}, which corresponds to 8.3 kW g^{-1} per watt·cm^{-2} of illumination light (note that the SAR is proportional to the power while it decreases with the concentration). This value is in the order of the highest obtained SAR for PVP/DMF-synthesized nanostars around 9.1 kW g^{-1} at 1 W cm^{-2}.[3]

The photothermal conversion efficiency, η, was obtained from the thermograms as indicated in the Experimental Section (Figure 5c). Interestingly, a clear increase in η is observed with the increase in Au size for the case of JNSs and also of the JNSs with respect to the JNSphs. On the other hand, as expected, no big differences are observed with varying sizes of the Fe_3O_4 component; the changes in the nanostar size and shape among the different sets play the most important role. The extinction coefficient, ε (capacity to interact with light at a given concentration), and η (capacity to transform the interaction light into heat) are the two parameters that govern the performance in terms of ΔT_{max} and SAR. In our case, both hyperthermia parameters follow a similar trend as a function of ε and η, producing a clear synergy toward the best performance of large JNSs when compared to small JNSs of JNSphs. This is easily visible when comparing the ΔT_{max} and SAR of Figure 5b with η of Figure 5c or the almost linear trend of ΔT_{max} and SAR vs ε of Figures 5d and S13, respectively, and it reflects the importance of the structure parameters, size and shape, on the photothermal performance.

Regarding the best choice for dual magneto- and photothermia, the final hyperthermia effect, in terms of SAR, is cumulative, i.e., the final SAR corresponds to the sum of the magnetothermia and photothermia SARs, as has been previously shown.[8,23] Thus, it is evidenced that the NPs with 30 nm iron oxide and bigger NSs, C.1, are the best choice in terms of SAR, both for the maximum attainable and for the one under biological safety limits. The presence of Au is beneficial for the magnetothermal effect, while the size of iron oxide does not seem to negatively influence the photothermal effect. Moreover, as the relative mass of the two components also changes with the component sizes, the NSs component could be decreased to have a better balance of Fe_3O_4:Au relative components and favor the lower capacity of the magnetothermia with still adequate photothermia. In that case, C.2 would be a well-balanced choice for dual-modality with additional magnetic guiding and contrast for imaging capabilities.

CONCLUSIONS

Briefly, a challenging strategy was followed to build a library of multicomponent heterostructures by tuning the size and morphology of multicomponent Janus Au:Fe_3O_4 NPs. This library was used to study the rules for generating superior plasmonic and photothermal efficiency in biological environments. The developed Au:Fe_3O_4 heterodimers, JNSs, and novel JNSphs showed structural and functional heating properties by an alternating magnetic field and a near-infrared (NIR) laser stimulation, achieving highly efficient heat conversion for both modalities. In a direct comparison, the evaluation of the heating efficiency for the different JNPs in water suspension demonstrated that the ones with bigger iron oxide components produced better magnetothermia performance, while the presence of Au improved this effect in all cases and where the Au shape could also give rise to small changes to tune the response. Values of SAR close to 3 kW g^{-1} were obtained for the best case and of 0.48 kW g^{-1} when $H \times f$ Hergt's limit was applied. On the other hand, JNSs with large-sized Au component were the best-performing ones to produce high SAR and temperature increments in photothermia. SAR values up to 8.3 kW g^{-1} per W cm^{-2} of light were obtained in this case. Additionally, noticeable differences appear in the photothermal conversion efficiency, which follows trends similar to those of the molar extinction coefficient, contributing positively to better performance. The results shown here, of the Janus design of multifunctional Au−Fe_3O_4 NPs, open the door to producing an efficient magnetic and plasmonic hybrid agent, in which the synergistic effect can help lower the therapeutic doses of NPs with appropriate magnetic field and frequency, as well as laser power.

ASSOCIATED CONTENT

Supporting Information

The Supporting Information is available free of charge at https://pubs.acs.org/doi/10.1021/acsanm.3c03818.

Synthesis parameters; XRD; example of SAR_{limit} fitting; description of the $SAR_{photothermia}$ and η analysis; UV−vis−NIR absorbance spectra of heterodimers; M−H loops of Au−Fe_3O_4 Janus NPs before and after etching the Au component obtained at 143 and 732 kHz; SAR as a function of the magnetic field of Au−Fe_3O_4 heterodimers before and after etching at 143 and 732 kHz; TEM images and comparative magnetic SAR of every single size of Au−Fe_3O_4 heterodimers before and after Au etching at three frequencies [143, 350, and 732 kHz]; SAR of Au−Fe_3O_4 JNPs as a function of the magnetic field in the range [0−80 mT] at 143 and 732 kHz and comparative SAR among different NPs; SAR per frequency as a function of the magnetic field in the range [0−80 mT] at three frequencies [143, 350, and 732 kHz] among different Janus NPs; maximum attainable SAR limit under biological safety conditions for all samples; and SAR values for different fittings (PDF)

AUTHOR INFORMATION

Corresponding Author

Javier Reguera − *BCMaterials, Basque Center for Materials, Applications, and Nanostructures, UPV/EHU Science Park, Leioa 48940, Spain;* orcid.org/0000-0001-5110-5361; Email: javier.reguera@bcmaterials.net

Authors

Esraa Samy Abu Serea − *BCMaterials, Basque Center for Materials, Applications, and Nanostructures, UPV/EHU Science Park, Leioa 48940, Spain*

Iñaki Orue − *SGIker Medidas Magnéticas, Universidad del País Vasco (UPV/EHU), 48940 Leioa, Spain*

José Ángel García − *Departamento de Física, Universidad del País Vasco (UPV/EHU), 48940 Leioa, Spain*

Senentxu Lanceros-Méndez − *BCMaterials, Basque Center for Materials, Applications, and Nanostructures, UPV/EHU Science Park, Leioa 48940, Spain; Ikerbasque, Basque Foundation for Science Bilbao, 48009 Bilbao, Spain;* orcid.org/0000-0001-6791-7620

Complete contact information is available at: https://pubs.acs.org/10.1021/acsanm.3c03818

Author Contributions

E.S.A: Investigation, visualization, formal analysis, writing—original draft. I.O: Methodology, validation, writing—review and editing. J.A.G: Formal analysis, resources, writing—review and editing, validation. S.L.M: Writing—review and editing; funding acquisition J.R: Conceptualization, methodology, supervision, validation, formal analysis, writing—review and editing; funding acquisition.

Notes

The authors declare no competing financial interest.

■ ACKNOWLEDGMENTS

The authors thank funding from the Spanish State Research Agency (AEI) through the project PID2019-106099RB-C43/AEI/10.13039/501100011033, PID2022-139467OB-I00 and the Basque Government under the ELKARTEK program, KK-2021/00124. The authors also thank the technical support of SGIker (UPV/EHU).

■ REFERENCES

(1) Moroz, P.; Jones, S. K.; Gray, B. N. Status of Hyperthermia in the Treatment of Advanced Liver Cancer. *J. Surg. Oncol.* **2001**, *77* (4), 259−269.

(2) Ahmed, M.; Goldberg, S. N. Thermal Ablation Therapy for Hepatocellular Carcinoma. *J. Vasc. Interv. Radiol.* **2002**, *13* (9), S231−S243.

(3) Espinosa, A.; Silva, A. K. A.; Sánchez-Iglesias, A.; Grzelczak, M.; Péchoux, C.; Desboeufs, K.; Liz-Marzán, L. M.; Wilhelm, C. Cancer Cell Internalization of Gold Nanostars Impacts Their Photothermal Efficiency In Vitro and In Vivo: Toward a Plasmonic Thermal Fingerprint in Tumoral Environment. *Adv. Healthcare Mater.* **2016**, *5* (9), 1040−1048.

(4) Habash, R. W. Y.; Bansal, R.; Krewski, D.; Alhafid, H. T. Thermal Therapy, Part 2: Hyperthermia Techniques. *Crit. Rev. Bioeng.* **2006**, *34* (6), 491−542.

(5) Castrén-Persons, M.; Schröder, T.; Rämö, O. J.; Puolakkainen, P.; Lehtonen, E. Contact Nd:YAG Laser Potentiates the Tumor Cell Killing Effect of Hyperthermia. *Lasers Surg. Med.* **1991**, *11* (6), 595−600.

(6) Seki, T.; Wakabayashi, M.; Nakagawa, T.; Imamura, M.; Tamai, T.; Nishimura, A.; Yamashiki, N.; Okamura, A.; Inoue, K. Percutaneous Microwave Coagulation Therapy for Patients with Small Hepatocellular Carcinoma: Comparison with Percutaneous Ethanol Injection Therapy. *Cancer* **1999**, *85* (8), 1694−1702.

(7) Jolesz, F. A. MRI-Guided Focused Ultrasound Surgery. *Annu. Rev. Med.* **2009**, *60* (1), 417−430.

(8) Espinosa, A.; Di Corato, R.; Kolosnjaj-Tabi, J.; Flaud, P.; Pellegrino, T.; Wilhelm, C. Duality of Iron Oxide Nanoparticles in Cancer Therapy: Amplification of Heating Efficiency by Magnetic Hyperthermia and Photothermal Bimodal Treatment. *ACS Nano* **2016**, *10* (2), 2436−2446.

(9) Ovejero, J. G.; Morales, I.; De La Presa, P.; Mille, N.; Carrey, J.; Garcia, M. A.; Hernando, A.; Herrasti, P. Hybrid Nanoparticles for Magnetic and Plasmonic Hyperthermia. *Phys. Chem. Chem. Phys.* **2018**, *20* (37), 24065−24073.

(10) Yan, H.; Shang, W.; Sun, X.; Zhao, L.; Wang, J.; Xiong, Z.; Yuan, J.; Zhang, R.; Huang, Q.; Wang, K.; Li, B.; Tian, J.; Kang, F.; Feng, S. S. All-in-One" Nanoparticles for Trimodality Imaging-Guided Intracellular Photo-Magnetic Hyperthermia Therapy under Intravenous Administration. *Adv. Funct. Mater.* **2018**, *28* (9), 1705710.

(11) Nguyen, T. T.; Mammeri, F.; Ammar, S. Iron Oxide and Gold Based Magneto-Plasmonic Nanostructures for Medical Applications: A Review. *Nanomaterials* **2018**, *8* (3), 149.

(12) Xu, Z.; Hou, Y.; Sun, S. Magnetic Core/Shell Fe_3O_4/Au and Fe_3O_4/Au/Ag Nanoparticles with Tunable Plasmonic Properties. *J. Am. Chem. Soc.* **2007**, *129* (28), 8698−8699.

(13) Lu, Q.; Dai, X.; Zhang, P.; Tan, X.; Zhong, Y.; Yao, C.; Song, M.; Song, G.; Zhang, Z.; Peng, G.; Guo, Z.; Ge, Y.; Zhang, K.; Li, Y. Fe_3O_4@Au Composite Magnetic Nanoparticles Modified with Cetuximab for Targeted Magneto-Photothermal Therapy of Glioma Cells. *Int. J. Nanomed.* **2018**, *13*, 2491−2505.

(14) Vallejo-Fernandez, G.; Whear, O.; Roca, A. G.; Hussain, S.; Timmis, J.; Patel, V.; O'Grady, K. Mechanisms of Hyperthermia in Magnetic Nanoparticles. *J. Phys. D: Appl. Phys.* **2013**, *46* (31), 312001.

(15) García-Hevia, L.; Casafont, Í.; Oliveira, J.; Terán, N.; Fanarraga, M. L.; Gallo, J.; Bañobre-López, M. Magnetic Lipid Nanovehicles Synergize the Controlled Thermal Release of Chemotherapeutics with Magnetic Ablation While Enabling Non-Invasive Monitoring by MRI for Melanoma Theranostics. *Bioact. Mater.* **2022**, *8*, 153−164.

(16) Datta, N. R.; Kok, H. P.; Crezee, H.; Gaipl, U. S.; Bodis, S. Integrating Loco-Regional Hyperthermia Into the Current Oncology Practice: SWOT and TOWS Analyses. *Front. Oncol.* **2020**, *10*, 819.

(17) Guardia, P.; Di Corato, R.; Lartigue, L.; Wilhelm, C.; Espinosa, A.; Garcia-Hernandez, M.; Gazeau, F.; Manna, L.; Pellegrino, T. Water-Soluble Iron Oxide Nanocubes with High Values of Specific Absorption Rate for Cancer Cell Hyperthermia Treatment. *ACS Nano* **2012**, *6* (4), 3080−3091.

(18) Nica, V.; Caro, C.; Páez-Muñoz, J. M.; Leal, M. P.; Garcia-Martin, M. L. Bi-Magnetic Core-Shell CoFe2O4@MnFe2O4 Nanoparticles for In Vivo Theranostics. *Nanomaterials* **2020**, *10* (5), 907.

(19) Hakami, T. M.; Davarpanah, A. M.; Rahdar, A.; Barrett, S. D. Structural and Magnetic Study and Cytotoxicity Evaluation of Tetra-Metallic Nanoparticles of Co0.5Ni0.5CrxFe2-XO4 Prepared by Co-Precipitation. *J. Mol. Struct.* **2018**, *1165*, 344−348.

(20) Storozhuk, L.; Besenhard, M. O.; Mourdikoudis, S.; LaGrow, A. P.; Lees, M. R.; Tung, L. D.; Gavriilidis, A.; Thanh, N. T. K. Stable Iron Oxide Nanoflowers with Exceptional Magnetic Heating Efficiency: Simple and Fast Polyol Synthesis. *ACS Appl. Mater. Interfaces* **2021**, *13* (38), 45870−45880.

(21) Lartigue, L.; Innocenti, C.; Kalaivani, T.; Awwad, A.; Sanchez Duque, M. D. M.; Guari, Y.; Larionova, J.; Guérin, C.; Montero, J. L. G.; Barragan-Montero, V.; Arosio, P.; Lascialfari, A.; Gatteschi, D.; Sangregorio, C. Water-Dispersible Sugar-Coated Iron Oxide Nanoparticles. An Evaluation of Their Relaxometric and Magnetic Hyperthermia Properties. *J. Am. Chem. Soc.* **2011**, *133* (27), 10459−10472.

(22) Christou, E.; Pearson, J. R.; Beltrán, A. M.; Fernández-Afonso, Y.; Gutiérrez, L.; de la Fuente, J. M.; Gámez, F.; García-Martín, M. L.; Caro, C. Iron-Gold Nanoflowers: A Promising Tool for Multimodal Imaging and Hyperthermia Therapy. *Pharmaceutics* **2022**, *14* (3), 636.

(23) Espinosa, A.; Reguera, J.; Curcio, A.; Muñoz-Noval, Á.; Kuttner, C.; Van de Walle, A.; Liz-Marzán, L. M.; Wilhelm, C. Janus Magnetic-Plasmonic Nanoparticles for Magnetically Guided and Thermally Activated Cancer Therapy. *Small* **2020**, *16* (11), 1904960.

(24) Mishra, S. K.; Kannan, S. A Bimetallic Silver-Neodymium Theranostic Nanoparticle with Multimodal NIR/MRI/CT Imaging and Combined Chemo-Photothermal Therapy. *Inorg. Chem.* **2017**, *56* (19), 12054−12066.

(25) Rincón-Iglesias, M.; Rodrigo, I.; B Berganza, L.; Serea, E. S. A.; Plazaola, F.; Lanceros-Méndez, S.; Lizundia, E.; Reguera, J. Core-Shell Fe_3O_4@Au Nanorod-Loaded Gels for Tunable and Anisotropic Magneto- and Photothermia. *ACS Appl. Mater. Interfaces* **2022**, *14* (5), 7130−7140.

(26) Nemati, Z.; Alonso, J.; Rodrigo, I.; Das, R.; Garaio, E.; García, J. Á.; Orue, I.; Phan, M. H.; Srikanth, H. Improving the Heating Efficiency of Iron Oxide Nanoparticles by Tuning Their Shape and Size. *J. Phys. Chem. C* **2018**, *122* (4), 2367−2381.

(27) Bohren, C. F. *Absorption and Scattering of Light by Small Particles*; Wiley VCH, 1983..

(28) Vines, J. B.; Yoon, J. H.; Ryu, N. E.; Lim, D. J.; Park, H. Gold Nanoparticles for Photothermal Cancer Therapy. *Front. Chem.* **2019**, *7*, 167.

https://doi.org/10.1021/acsanm.3c03818
ACS Appl. Nano Mater. 2023, 6, 18466−18479

(29) Jauffred, L.; Samadi, A.; Klingberg, H.; Bendix, P. M.; Oddershede, L. B. Plasmonic Heating of Nanostructures. *Chem. Rev.* **2019**, *119* (13), 8087−8130.
(30) Siegel, A. L.; Baker, G. A. Bespoke Nanostars: Synthetic Strategies, Tactics, and Uses of Tailored Branched Gold Nanoparticles. *Nanoscale Adv.* **2021**, *3* (14), 3980−4004.
(31) de Puig, H.; Tam, J. O.; Yen, C.-W.; Gehrke, L.; Hamad-Schifferli, K. Extinction Coefficient of Gold Nanostars. *J. Phys. Chem. C* **2015**, *119* (30), 17408−17415.
(32) Trigari, S.; Rindi, A.; Margheri, G.; Sottini, S.; Dellepiane, G.; Giorgetti, E. Synthesis and Modelling of Gold Nanostars with Tunable Morphology and Extinction Spectrum. *J. Mater. Chem.* **2011**, *21* (18), 6531.
(33) Wydra, R. J.; Oliver, C. E.; Anderson, K. W.; Dziubla, T. D.; Hilt, J. Z. Accelerated Generation of Free Radicals by Iron Oxide Nanoparticles in the Presence of an Alternating Magnetic Field. *RSC Adv.* **2015**, *5* (24), 18888−18893.
(34) Van de Walle, A.; Kolosnjaj-Tabi, J.; Lalatonne, Y.; Wilhelm, C. Ever-Evolving Identity of Magnetic Nanoparticles within Human Cells: The Interplay of Endosomal Confinement, Degradation, Storage, and Neocrystallization. *Acc. Chem. Res.* **2020**, *53* (10), 2212−2224.
(35) Mazuel, F.; Espinosa, A.; Radtke, G.; Bugnet, M.; Neveu, S.; Lalatonne, Y.; Botton, G. A.; Abou-Hassan, A.; Wilhelm, C. Magneto-Thermal Metrics Can Mirror the Long-Term Intracellular Fate of Magneto-Plasmonic Nanohybrids and Reveal the Remarkable Shielding Effect of Gold. *Adv. Funct. Mater.* **2017**, *27* (9), 1605997.
(36) Díez, A.; Rincón-Iglesias, M.; Lanceros-Méndez, S.; Reguera, J.; Lizundia, E. Multicomponent Magnetic Nanoparticle Engineering: The Role of Structure-Property Relationship in Advanced Applications. *Mater. Today Chem.* **2022**, *26*, 101220.
(37) Reguera, J.; Jiménez de Aberasturi, D.; Henriksen-Lacey, M.; Langer, J.; Espinosa, A.; Szczupak, B.; Wilhelm, C.; Liz-Marzán, L. M. Janus Plasmonic-Magnetic Gold-Iron Oxide Nanoparticles as Contrast Agents for Multimodal Imaging. *Nanoscale* **2017**, *9* (27), 9467−9480.
(38) Reguera, J.; Flora, T.; Winckelmans, N.; Rodríguez-Cabello, J. C.; Bals, S. Self-Assembly of Janus Au:Fe_3O_4 Branched Nanoparticles. From Organized Clusters to Stimuli-Responsive Nanogel Superstructures. *Nanoscale Adv.* **2020**, *2* (6), 2525−2530.
(39) Reguera, J.; Jiménez de Aberasturi, D.; Winckelmans, N.; Langer, J.; Bals, S.; Liz-Marzán, L. M. Synthesis of Janus Plasmonic-Magnetic, Star-Sphere Nanoparticles, and Their Application in SERS Detection. *Faraday Discuss.* **2016**, *191*, 47−59.
(40) López-Méndez, R.; Reguera, J.; Fromain, A.; Serea, E. S. A.; Céspedes, E.; Terán, F.; Parente, A.; García, M. A.; Fonda, E.; Camarero, J.; Wilhelm, C.; Muñoz-Noval, A.; Espinosa, A. X-Ray Nanothermometry of Nanoparticles in Tumor-Mimicking Tissues under Photothermia. *Adv. Healthcare Mater.* **2023**, 2301863.
(41) Guardia, P.; Nitti, S.; Materia, M. E.; Pugliese, G.; Yaacoub, N.; Greneche, J. M.; Lefevre, C.; Manna, L.; Pellegrino, T. Gold-Iron Oxide Dimers for Magnetic Hyperthermia: The Key Role of Chloride Ions in the Synthesis to Boost the Heating Efficiency. *J. Mater. Chem. B* **2017**, *5* (24), 4587−4594.
(42) Yu, H.; Chen, M.; Rice, P. M.; Wang, S. X.; White, R. L.; Sun, S. Dumbbell-like Bifunctional Au-Fe_3O_4 Nanoparticles. *Nano Lett.* **2005**, *5* (2), 379−382.
(43) Lin, C. A. J.; Sperling, R. A.; Li, J. K.; Yang, T. Y.; Li, P. Y.; Zanella, M.; Chang, W. H.; Parak, W. J. Design of an Amphiphilic Polymer for Nanoparticle Coating and Functionalization. *Small* **2008**, *4* (3), 334−341.
(44) Rodrigo, I.; Castellanos-Rubio, I.; Garaio, E.; Arriortua, O. K.; Insausti, M.; Orue, I.; García, J. Á.; Plazaola, F. Exploring the Potential of the Dynamic Hysteresis Loops via High Field, High Frequency and Temperature Adjustable AC Magnetometer for Magnetic Hyperthermia Characterization. *Int. J. Hyperthermia* **2020**, *37* (1), 976−991.
(45) Andreu, I.; Natividad, E. Accuracy of Available Methods for Quantifying the Heat Power Generation of Nanoparticles for Magnetic Hyperthermia. *Int. J. Hyperthermia* **2013**, *29* (8), 739−751.
(46) Jordan, A.; Wust, P.; Fähling, H.; John, W.; Hinz, A.; Felix, R. Inductive Heating of Ferrimagnetic Particles and Magnetic Fluids: Physical Evaluation of Their Potential for Hyperthermia. *Int. J. Hyperthermia* **2009**, *25* (7), 499−511.
(47) Rodrigues, H. F.; Capistrano, G.; Bakuzis, A. F. In Vivo Magnetic Nanoparticle Hyperthermia: A Review on Preclinical Studies, Low-Field Nano-Heaters, Noninvasive Thermometry and Computer Simulations for Treatment Planning. *Int. J. Hyperthermia* **2020**, *37* (3), 76−99.
(48) Stauffer, P. R. Physics of Thermal Therapy: Fundamentals and Clinical Applications. *Med. Phys.* **2013**, *40*, 067302.
(49) Castellanos-Rubio, I.; Barón, A.; Luis-Lizarraga, O.; Rodrigo, I.; de Muro, I. G.; Orue, I.; Martínez-Martínez, V.; Castellanos-Rubio, A.; López-Arbeloa, F.; Insausti, M. Efficient Magneto-Luminescent Nanosystems Based on Rhodamine-Loaded Magnetite Nanoparticles with Optimized Heating Power and Ideal Thermosensitive Fluorescence. *ACS Appl. Mater. Interfaces* **2022**, *14* (44), 50033−50044.
(50) Roper, D. K.; Ahn, W.; Hoepfner, M. Microscale Heat Transfer Transduced by Surface Plasmon Resonant Gold Nanoparticles. *J. Phys. Chem. C* **2007**, *111* (9), 3636−3641.
(51) Wildeboer, R. R.; Southern, P.; Pankhurst, Q. A. On the Reliable Measurement of Specific Absorption Rates and Intrinsic Loss Parameters in Magnetic Hyperthermia Materials. *J. Phys. D: Appl. Phys.* **2014**, *47* (49), 495003.
(52) Castellanos-Rubio, I.; Arriortua, O.; Iglesias-Rojas, D.; Barón, A.; Rodrigo, I.; Marcano, L.; Garitaonandia, J. S.; Orue, I.; Fdez-Gubieda, M. L.; Insausti, M. A Milestone in the Chemical Synthesis of Fe_3O_4 Nanoparticles: Unreported Bulklike Properties Lead to a Remarkable Magnetic Hyperthermia. *Chem. Mater.* **2021**, *33* (22), 8693−8704.
(53) Schick, I.; Gehrig, D.; Montigny, M.; Balke, B.; Panthöfer, M.; Henkel, A.; Laquai, F.; Tremel, W. Effect of Charge Transfer in Magnetic-Plasmonic Au@MO_x (M = Mn, Fe) Heterodimers on the Kinetics of Nanocrystal Formation. *Chem. Mater.* **2015**, *27* (13), 4877−4884.
(54) Litti, L.; Reguera, J.; García de Abajo, F. J.; Meneghetti, M.; Liz-Marzán, L. M. Manipulating Chemistry through Nanoparticle Morphology. *Nanoscale Horiz.* **2020**, *5* (1), 102−108.
(55) Bastús, N. G.; Comenge, J.; Puntes, V. Kinetically Controlled Seeded Growth Synthesis of Citrate-Stabilized Gold Nanoparticles of up to 200 nm: Size Focusing versus Ostwald Ripening. *Langmuir* **2011**, *27* (17), 11098−11105.
(56) Hao, F.; Nehl, C. L.; Hafner, J. H.; Nordlander, P. Plasmon Resonances of a Gold Nanostar. *Nano Lett.* **2007**, *7* (3), 729−732.
(57) Nemati, Z.; Alonso, J.; Martinez, L. M.; Khurshid, H.; Garaio, E.; Garcia, J. A.; Phan, M. H.; Srikanth, H. Enhanced Magnetic Hyperthermia in Iron Oxide Nano-Octopods: Size and Anisotropy Effects. *J. Phys. Chem. C* **2016**, *120* (15), 8370−8379.
(58) Hemery, G.; Keyes, A. C.; Garaio, E.; Rodrigo, I.; Garcia, J. A.; Plazaola, F.; Garanger, E.; Sandre, O. Tuning Sizes, Morphologies, and Magnetic Properties of Monocore Versus Multicore Iron Oxide Nanoparticles through the Controlled Addition of Water in the Polyol Synthesis. *Inorg. Chem.* **2017**, *56* (14), 8232−8243.
(59) Das, R.; Alonso, J.; Nemati Porshokouh, Z.; Kalappattil, V.; Torres, D.; Phan, M. H.; Garaio, E.; García, J. Á.; Sanchez Llamazares, J. L.; Srikanth, H. Tunable High Aspect Ratio Iron Oxide Nanorods for Enhanced Hyperthermia. *J. Phys. Chem. C* **2016**, *120* (18), 10086−10093.
(60) Garaio, E.; Sandre, O.; Collantes, J.-M.; Garcia, J. A.; Mornet, S.; Plazaola, F. Specific Absorption Rate Dependence on Temperature in Magnetic Field Hyperthermia Measured by Dynamic Hysteresis Losses (Ac Magnetometry). *Nanotechnology* **2015**, *26* (1), 015704.
(61) Garaio, E.; Collantes, J. M.; Plazaola, F.; Garcia, J. A.; Castellanos-Rubio, I. A Multifrequency Eletromagnetic Applicator with an Integrated AC Magnetometer for Magnetic Hyperthermia Experiments. *Meas. Sci. Technol.* **2014**, *25* (11), 115702.
(62) Mohapatra, J.; Zeng, F.; Elkins, K.; Xing, M.; Ghimire, M.; Yoon, S.; Mishra, S. R.; Liu, J. P. Size-Dependent Magnetic and

Inductive Heating Properties of Fe_3O_4 Nanoparticles: Scaling Laws across the Superparamagnetic Size. *Phys. Chem. Chem. Phys.* **2018**, *20* (18), 12879−12887.
(63) Mehdaoui, B.; Meffre, A.; Carrey, J.; Lachaize, S.; Lacroix, L. M.; Gougeon, M.; Chaudret, B.; Respaud, M. Optimal Size of Nanoparticles for Magnetic Hyperthermia: A Combined Theoretical and Experimental Study. *Adv. Funct. Mater.* **2011**, *21* (23), 4573−4581.
(64) Kandasamy, G.; Maity, D. Recent Advances in Superparamagnetic Iron Oxide Nanoparticles (SPIONs) for in Vitro and in Vivo Cancer Nanotheranostics. *Int. J. Pharm.* **2015**, *496* (2), 191−218.
(65) Boal, A. K.; Frankamp, B. L.; Uzun, O.; Tuominen, M. T.; Rotello, V. M. Modulation of Spacing and Magnetic Properties of Iron Oxide Nanoparticles through Polymer-Mediated "Bricks and Mortar" Self-Assembly. *Chem. Mater.* **2004**, *16* (17), 3252−3256.
(66) Dössel, O.; Bohnert, J. Safety Considerations for Magnetic Fields of 10 MT to 100 MT Amplitude in the Frequency Range of 10 kHz to 100 kHz for Magnetic Particle Imaging. *Biomed. Eng.* **2013**, *58* (6), 611−621.
(67) Herrero de la Parte, B.; Rodrigo, I.; Gutiérrez-Basoa, J.; Iturrizaga Correcher, S.; Mar Medina, C.; Echevarría-Uraga, J. J.; Garcia, J. A.; Plazaola, F.; García-Alonso, I. Proposal of New Safety Limits for In Vivo Experiments of Magnetic Hyperthermia Antitumor Therapy. *Cancers* **2022**, *14* (13), 3084.
(68) Kossatz, S.; Ludwig, R.; Dähring, H.; Ettelt, V.; Rimkus, G.; Marciello, M.; Salas, G.; Patel, V.; Teran, F. J.; Hilger, I. High Therapeutic Efficiency of Magnetic Hyperthermia in Xenograft Models Achieved with Moderate Temperature Dosages in the Tumor Area. *Pharm. Res.* **2014**, *31* (12), 3274−3288.
(69) Atkinson, W. J.; Brezovich, I. A.; Chakraborty, D. P. Usable Frequencies in Hyperthermia with Thermal Seeds. *IEEE Trans. Biomed. Eng.* **1984**, *BME-31* (1), 70−75.
(70) Wust, P.; Gneveckow, U.; Wust, P.; Gneveckow, U.; Johannsen, M.; Böhmer, D.; Henkel, T.; Kahmann, F.; Sehouli, J.; Felix, R.; et al. Magnetic Nanoparticles for Interstitial Thermotherapy - Feasibility, Tolerance and Achieved Temperatures. *Int. J. Hyperthermia* **2006**, *22* (8), 673−685.
(71) Jefremovas, E. M.; Gandarias, L.; Rodrigo, I.; Marcano, L.; Gruttner, C.; Garcia, J. A.; Garayo, E.; Orue, I.; Garcia-Prieto, A.; Muela, A.; Fernandez-Gubieda, M. L.; Alonso, J.; Barquin, L. F. Nanoflowers versus Magnetosomes: Comparison between Two Promising Candidates for Magnetic Hyperthermia Therapy. *IEEE Access* **2021**, *9*, 99552−99561.
(72) Ding, X.; Liow, C. H.; Zhang, M.; Huang, R.; Li, C.; Shen, H.; Liu, M.; Zou, Y.; Gao, N.; Zhang, Z.; Li, Y.; Wang, Q.; Li, S.; Jiang, J. Surface Plasmon Resonance Enhanced Light Absorption and Photothermal Therapy in the Second Near-Infrared Window. *J. Am. Chem. Soc.* **2014**, *136* (44), 15684−15693.
(73) Jacques, S. L. Laser-Tissue Interactions: Photochemical, Photothermal, and Photomechanical. *Surg. Clin. North Am.* **1992**, *72* (3), 531−558.
(74) Bashkatov, A. N.; Genina, E. A.; Kochubey, V. I.; Tuchin, V. V. Optical Properties of Human Skin, Subcutaneous and Mucous Tissues in the Wavelength Range from 400 to 2000 nm. *J. Phys. D Appl. Phys.* **2005**, *38* (15), 2543−2555.
(75) Bucharskaya, A.; Maslyakova, G.; Terentyuk, G.; Yakunin, A.; Avetisyan, Y.; Bibikova, O.; Tuchina, E.; Khlebtsov, B.; Khlebtsov, N.; Tuchin, V. Towards Effective Photothermal/Photodynamic Treatment Using Plasmonic Gold Nanoparticles. *Int. J. Mol. Sci.* **2016**, *17* (8), 1295.

https://doi.org/10.1021/acsanm.3c03818
ACS Appl. Nano Mater. 2023, 6, 18466−18479